Error Models for Long-Distance Qubit Teleportation

Brent J. Yen and Jeffrey H. Shapiro, *Fellow, IEEE*

Invited Paper

***Abstract*—A recent proposal for realizing long-distance, high-fidelity qubit teleportation is reviewed. This quantum communication architecture relies on an ultrabright source of polarization-entangled photons plus a pair of trapped-atom quantum memories, and it is compatible with long-distance transmission over standard telecommunication fiber. Models are developed for assessing the effects of amplitude, phase, and frequency errors in the entanglement source, as well as fiber loss and imperfect polarization restoration, on the throughput and fidelity of the system.**

***Index Terms*—Parametric amplifiers, polarization entanglement, quantum communication, teleportation.**

I. Introduction

A TEAM OF researchers from the Massachusetts Institute of Technology (MIT), Cambridge, MA, and Northwestern University (NU), Evanston, IL, has proposed a quantum communication architecture [1] that permits long-distance high-fidelity teleportation using the Bennett *et al.* singlet-state protocol [2]. This architecture uses a novel ultrabright source of polarization-entangled photon pairs [3] and trapped-atom quantum memories [4] in which all four Bell states can be measured. By means of quantum-state frequency conversion and time-division multiplexed polarization restoration, it is able to employ standard telecommunication fiber for long-distance transmission of the polarization-entangled photons. This paper studies the effects of source and fiber-transmission errors on the throughput and fidelity achieved by the MIT/NU system.

Section II reviews the MIT/NU architecture, to establish the foundation for the error models that will follow. It introduces the lumped-element model for the dual optical parametric amplifier (dual-OPA) entanglement source, describes how quantum-state frequency conversion and time-division-multiplexed polarization restoration permit the use of standard telecommunication fiber, and discusses the functioning of the trapped-atom quantum memories. Section III presents our fiber-transmission model, which accounts for propagation loss and imperfect polarization restoration. Section IV generalizes the cavity-loading analysis from [1] to include nonidealities in the source and fiber transmission. Section V develops the single-photon error models implied by the result of this loading analysis, i.e., by the joint state of the loaded memory cavities. The throughput and fidelity assessments that follow from these error models appear in Section VI.

Manuscript received March 15, 2003; revised August 21, 2003. This work was supported by the DoD Multidisciplinary University Research Initiative (MURI) Program administered by the Army Research Office under Grant DAAD19-00-1-0177 and by the Quantum Information Science and Technology Program under Army Research Office Grant DAAD19-01-1-0647.

The authors are with the Department of Electrical Engineering and Computer Science and the Research Laboratory of Electronics, Massachusetts Institute of Technology, Cambridge, MA 02139-4307 USA (e-mail: jhs@mit.edu).

Digital Object Identifier 10.1109/JSTQE.2003.820906

Fig. 1. Schematic of long-distance quantum communication system: P = ultrabright narrowband source of polarization-entangled photon pairs; L = L km of standard telecommunication fiber; M = trapped-atom quantum memory.

II. MIT/NU Communication Architecture

The notion that a singlet state could be used to teleport a qubit is due to [2]. The transmitter and the receiver stations share the entangled qubits of a singlet state, $|\psi^-\rangle_{\rm TR} = (|0\rangle_{\rm T}|1\rangle_{\rm R} - |1\rangle_{\rm T}|0\rangle_{\rm R})/\sqrt{2}$, and the transmitter then accepts a message qubit, $|\psi\rangle_{\rm M} = \alpha|0\rangle_{\rm M} + \beta|1\rangle_{\rm M}$, leaving the message mode, the transmitter, and the receiver in the joint state $|\psi\rangle_{\rm M}|\psi^-\rangle_{\rm TR}$. Making the Bell-state measurements, $\{|\psi^\pm\rangle_{\rm MT} = (|1\rangle_{\rm M}|0\rangle_{\rm T} \pm |0\rangle_{\rm M}|1\rangle_{\rm T})/\sqrt{2}, |\phi^\pm\rangle_{\rm MT} = (|1\rangle_{\rm M}|1\rangle_{\rm T} \pm |0\rangle_{\rm M}|0\rangle_{\rm T})/\sqrt{2}\}$, on the joint message/transmitter system then yields the two bits of classical information that the receiver needs to transform its portion of the original singlet into a reproduction of the message qubit.

An initial experimental demonstration of teleportation using singlet states was performed by Bouwmeester *et al.* [5], [6], but only one of the Bell states was measured, the demonstration was a table-top experiment, and it did not include a quantum memory. The MIT/NU proposal for a singlet-based quantum communication system, which is shown in Fig. 1, remedies all of these limitations. It uses an ultrabright source of polarization-entangled photon pairs, formed by combining the outputs from two coherently-pumped, type-II phase-matched optical parametric amplifiers on a polarizing beam splitter. It transmits one photon from each pair down standard telecommunication fibers to a pair of trapped ^{87}Rb-atom quantum memories for storage and processing of this entanglement. One of these memories serves as the transmitter station and the other as the receiver station for qubit teleportation. We will devote the rest of this section to describing these basic components and their operation within the MIT/NU quantum communication architecture.

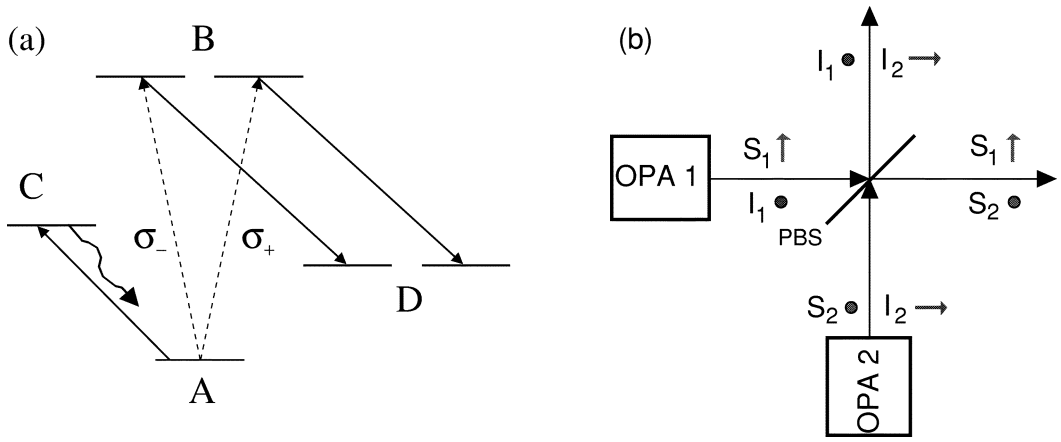

Fig. 2. Essential components of the singlet-state quantum communication system from Fig. 1. (a) Simplified energy-level diagram of the trapped rubidium atom quantum memory. The A-to-B transition occurs when a photon is absorbed. The B-to-D transition is coherently driven to enable storage in the long-lived D levels. The A-to-C cycling transition is used for nondestructive verification of a loading event. (b) Ultrabright narrowband source of polarization-entangled photon pairs. The polarizations $\hat{x}$ and $\hat{y}$ are denoted by arrows and bullets, respectively; PBS = polarizing beam splitter.

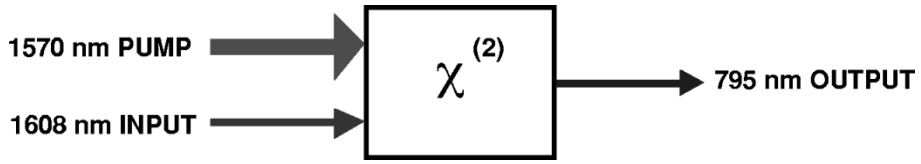

Fig. 3. Schematic diagram of quantum-state frequency conversion: a strong pump beam at 1570 nm converts a qubit photon received at 1608 nm (in the low-loss fiber transmission window) to a qubit photon at the 795 nm wavelength of the $^{87}\mathrm{Rb}$ quantum memory via a single-pass interaction in a second-order ($\chi^{(2)}$) nonlinear crystal.

A. Ultrabright Source of Polarization-Entangled Photons

The Fig. 1 system requires a source of entangled photons at the 795-nm line of its rubidium atom quantum memories. Furthermore, only those pairs within a narrow frequency band ($\sim$10 MHz) of the 795 nm line will successfully load the memory, so the Fig. 1 system places a premium on source brightness. Spontaneous parametric downconversion is the standard approach for generating polarization-entangled photons. It is so broadband ($\sim 10^{13}$ Hz), however, that its pair-generation rate in the narrow bandwidth needed for coupling into the rubidium atom is extremely low: $\sim$15 pairs/s in a 30-MHz bandwidth. The P block in Fig. 1 represents an ultrabright narrowband source [3], which is capable of producing 1.5×10^6 pairs/sec in a 30-MHz bandwidth by combining the signal and idler output beams from two doubly resonant type-II phase matched OPAs, as sketched in Fig. 2(b).

Quasi-phase-matching in periodically-poled nonlinear materials makes it possible to choose the OPA wavelength, for our polarization-entanglement source, to suit the application at hand. In particular, by using periodically-poled potassium titanyl phosphate (PPKTP), a quasi-phase-matched type-II nonlinear material, we can produce $\sim 10^6$ pairs/s at the 795 nm wavelength of the rubidium memory for direct memory-loading (i.e., local-storage) applications. For long-distance transmission to remotely located memories, we can use a different PPKTP crystal and pump wavelength to generate 10^6 pairs/s in the 1.55 μm wavelength low-loss fiber transmission window. After fiber propagation we shift the entanglement to the 795 nm wavelength needed for the rubidium-atom memory via quantum-state frequency conversion [7], [8], shown in Fig. 3.

In [3], we reported a lumped-element analysis for a continuous-wave, doubly-resonant, dual-OPA system with amplitude-matched, anti-phased, nondepleting pumps and no excess losses. We used that analysis in [1] to demonstrate that such an arrangement produces the high-brightness, narrowband singlet states needed for qubit teleportation. More recently, we have shown that a broadband traveling-wave treatment of a type-II phase matched, doubly-resonant, dual OPA system reproduces the lumped element results when the former is limited to a few cavity linewidths about a double resonance [9]. Because the trapped-atom quantum memory in the MIT/NU architecture will only respond to that portion of the dual-OPAs output that lies within a narrow spectral region about the 795 nm atomic line, we shall employ the lumped-element source theory in what follows. Because we are interested in the effects that pump amplitude, phase, and frequency errors will have on the throughput and fidelity of the teleportation system, we need to generalize somewhat the dual-OPA source model from [1], [3].

Following [10], we have that the equations of motion governing the intracavity annihilation operators, $\{\hat{a}_{k_j}(t) : k = S, I,\ j = 1, 2\}$, of the signal and idler modes for the jth OPA are

$$\left(\frac{\mathrm{d}}{\mathrm{d}t} + \Gamma\right)\hat{a}_{S_j}(t) = (-1)^{j-1} G_j \Gamma \hat{a}^{\dagger}_{I_j}(t) + \sqrt{2\gamma}\hat{A}^{\mathrm{IN}}_{S_j}(t) + \sqrt{2(\Gamma-\gamma)}\hat{A}^{v}_{S_j}(t) \quad (1)$$

$$\left(\frac{\mathrm{d}}{\mathrm{d}t} + \Gamma\right)\hat{a}_{I_j}(t) = (-1)^{j-1} G_j \Gamma \hat{a}^{\dagger}_{S_j}(t) + \sqrt{2\gamma}\hat{A}^{\mathrm{IN}}_{I_j}(t) + \sqrt{2(\Gamma-\gamma)}\hat{A}^{v}_{I_j}(t) \quad (2)$$

where $\{\hat{A}_{k_j}^{\mathrm{IN}}(t)e^{-i\omega_k t}, \hat{A}_{k_j}^{v}(t)e^{-i\omega_k t}\}$ are the positive-frequency, photon-units input field and OPA-cavity loss operators for the signal and idler fields, all of which are taken to be in their vacuum states. In these equations we have assumed that the two OPAs are phase matched at a double resonance which occurs for signal frequency ω_S and idler frequency ω_I. We have also assumed that all four OPA modes see identical cavities, with common linewidth Γ and output-coupling rate $\gamma \leq \Gamma$. To capture the effects of pump amplitude, phase, and frequency errors, we allow each OPA to have a different, complex-valued normalized pump strength G_j, where $|G_j|^2$ equals the pump power divided by the threshold power for oscillation, and we allow the center frequencies ω_S and ω_I to be detuned from frequency degeneracy by $\Delta\omega$ and $-\Delta\omega$, respectively. The $(-1)^{j-1}$ factors in these equations imply that $\arg(G_1) = \arg(G_2)$ corresponds to the antiphased pumping required for generating the polarization-entangled singlet state which is needed in the Bennett *et al.* teleportation protocol.

The OPAs output fields are given by

$$\hat{A}_{S_j}^{\mathrm{OPA}}(t) = \sqrt{2\gamma}\hat{a}_{S_j}(t) - \hat{A}_{S_j}^{\mathrm{IN}}(t) \tag{3}$$

$$\hat{A}_{I_j}^{\mathrm{OPA}}(t) = \sqrt{2\gamma}\hat{a}_{I_j}(t) - \hat{A}_{I_j}^{\mathrm{IN}}(t) \tag{4}$$

and it is the statistics of these output fields that characterize the quality of the dual-OPA as an entanglement source for use in teleportation.

Equations (1)–(4) are easily solved, in the frequency domain, yielding a pair of two-mode Bogoliubov transformations relating the input and output field operators for each OPA. These in turn imply that the OPAs produce signal and idler beams in zero-mean, entangled Gaussian states, which are completely characterized by the following normally ordered and phase-sensitive correlation functions

$$K_{\mathrm{OPA}_j}^{(n)}(\tau) = \left\langle \hat{A}_{k_j}^{\mathrm{OPA}\dagger}(t+\tau)\hat{A}_{k_j}^{\mathrm{OPA}}(t) \right\rangle = \frac{|G_j|\gamma}{2}\left[\frac{e^{-(1-|G_j|)\Gamma|\tau|}}{1-|G_j|} - \frac{e^{-(1+|G_j|)\Gamma|\tau|}}{1+|G_j|}\right] \tag{5}$$

and

$$K_{\mathrm{OPA}_j}^{(p)}(\tau) = \left\langle \hat{A}_{S_j}^{\mathrm{OPA}}(t+\tau)\hat{A}_{I_j}^{\mathrm{OPA}}(t) \right\rangle = \frac{G_j\gamma}{2}\left[\frac{e^{-(1-|G_j|)\Gamma|\tau|}}{1-|G_j|} + \frac{e^{-(1+|G_j|)\Gamma|\tau|}}{1+|G_j|}\right]. \tag{6}$$

B. Quantum-State Transmission Over Fiber

Successful singlet transmission requires that polarization not be degraded by the propagation process. Yet, propagation through standard telecommunication fiber produces random, slowly-varying (∼msec time scale) polarization variations, so a means for polarization restoration is required. The approach taken for polarization restoration in the MIT/NU architecture, shown schematically in Fig. 4, relies on time-division multiplexing (TDM). Time slices from the signal beams from the two OPAs are sent down one fiber in the same linear polarization but in nonoverlapping time slots, accompanied by a strong out-of-band pulse. By tracking and restoring the linear polarization of the strong pulse, we can restore the linear polarization of the signal-beam time slices at the far end of the fiber. After this linear-polarization restoration, we then reassemble a time-epoch of the full vector signal beam by delaying the first time slot and combining it on a polarizing beam splitter with the second time slot after the latter has had its linear polarization rotated by 90°. A similar procedure is performed to reassemble idler time-slices after they have propagated down the other fiber. This approach, which is inspired by the Bergman *et al.* two-pulse fiber-squeezing experiment [11], common-modes out the vast majority of the phase fluctuations and the polarization birefringence incurred in the fiber, permitting standard telecommunication fiber to be used in lieu of the lossier and much more expensive polarization-maintaining fiber.

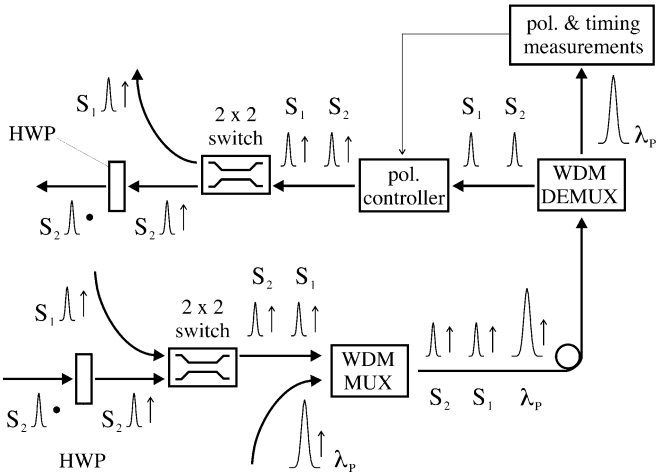

Fig. 4. Transmission of time-division multiplexed signal beams from OPAs 1 and 2 through an optical fiber. λ_p = pilot pulse, WDM MUX = wavelength-division multiplexer, WDM DEMUX = wavelength-division demultiplexer, HWP = half-wave plate.

C. Trapped-Atom Quantum Memory

Each M block in Fig. 1 is a quantum memory in which a single ultra-cold $^{87}\mathrm{Rb}$ atom (∼6 MHz linewidth) is confined by a far-off-resonance laser trap (FORT) in an ultra-high-vacuum chamber with cryogenic walls within a high-finesse (∼15-MHz linewidth) single-ended optical cavity. This memory can absorb a 795 nm photon, in an arbitrary polarization state, transferring the qubit from the photon to the degenerate B levels of Fig. 2(a) and thence to long-lived storage levels, by coherently driving the B-to-D transitions. (We are using abstract symbols here for the hyperfine levels of rubidium; see [4] for the actual atomic levels involved as well as a complete description of the memory and its operation.) With a liquid helium cryostat, so that the background pressure is less than 10^{-14} torr, the expected lifetime of the trapped rubidium atom will be more than an hour. Fluctuations in the residual magnetic field, however, will probably limit the atom's decoherence time to a few minutes.

By using optically off-resonant Raman (OOR) transitions, the Bell states of two atoms in a single vacuum-chamber trap can be converted to superposition states of one of the atoms. All four Bell measurements can then be made, sequentially, by detecting

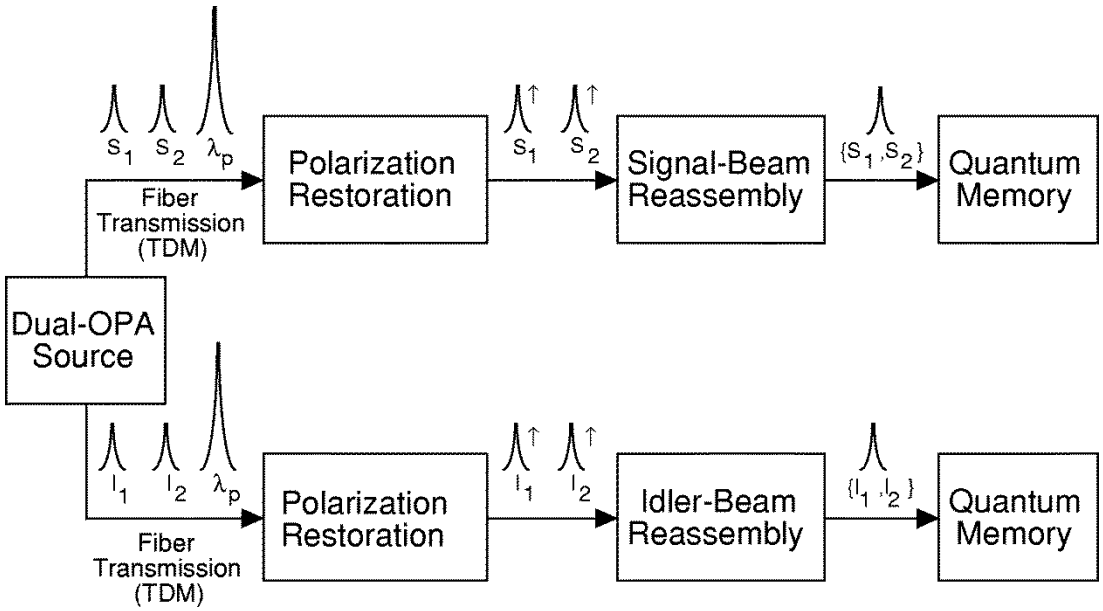

Fig. 5. Signal and idler beams from the dual-OPA polarization entanglement source are transmitted down optical fibers for loading into remote quantum memories.

the presence (or absence) of fluorescence as an appropriate sequence of OOR laser pulses is applied to the latter atom [4]. The Bell-measurement results in one memory can be sent to a distant memory, where at most two additional OOR pulses are needed to complete the Bennett *et al*. state transformation. The qubit stored in a trapped rubidium atom can be converted back into a photon by reversing the Raman excitation process that occurs during memory loading.

III. Fiber Transmission Error Model

In this section, we develop a model for propagation loss and imperfect polarization restoration in TDM transmission of polarization-entangled photons through a pair of optical fibers; see Fig. 5.

A. Propagation Loss

As suggested by Fig. 1, we will take the dual-OPA source to be equidistant from the two quantum memories, and thus we may assume that the signal and idler beams encounter the same transmission factor, $\eta_L < 1$, in propagation to their respective quantum memories. It is then easy to show that the effects of this propagation loss can be lumped into the source model itself, i.e., we can consider the fibers to be lossless by changing the dual-OPAs normally-ordered and phase-sensitive correlation functions to be

$$K^{(n)}_{\mathrm{OPA}_j}(\tau)=\frac{\eta_L|G_j|\gamma}{2}\left[\frac{e^{-(1-|G_j|)\Gamma|\tau|}}{1-|G_j|}-\frac{e^{-(1+|G_j|)\Gamma|\tau|}}{1+|G_j|}\right] \quad (7)$$

$$K^{(p)}_{\mathrm{OPA}_j}(\tau)=\frac{\eta_L G_j\gamma}{2}\left[\frac{e^{-(1-|G_j|)\Gamma|\tau|}}{1-|G_j|}+\frac{e^{-(1+|G_j|)\Gamma|\tau|}}{1+|G_j|}\right] \quad (8)$$

in lieu of the expressions from (5) and (6).

B. Imperfect Polarization Restoration

The narrowband nature of the dual-OPAs signal and idler beams, which obviates any issue of dispersive pulse spreading, combined with the short duration ($\sim 1\ \mu$sec [1]) of the TDM sequence compared to the msec time scale over which fiber fluctuations occur, imply that we need only concern ourselves with simple, time-independent polarization transformations for $\{\lambda_p, S_1, S_2\}$ on one fiber and $\{\lambda_p, I_1, I_2\}$ on the other fiber.[1] In particular, suppose we use the x polarization as the input to the fibers and

$$\hat{\boldsymbol{A}}_{k_j}(t)\equiv\left(\hat{A}^{\mathrm{OPA}}_{k_j}(t)\quad \hat{A}^{f}_{k_j}(t)\right)^T \quad (9)$$

to denote the vector field operators for the signal and idler time slots at the input to the fiber, where the y-polarized operators, $\{\hat{A}^{f}_{k_j}(t)\}$, are all in vacuum states. The corresponding vector field operators at the output of the fiber will then be given by

$$\hat{\boldsymbol{A}}'_{k_j}(t)=\mathcal{F}_k\left(\theta_k,\varphi_k,\varphi'_k,\psi_k\right)\hat{\boldsymbol{A}}_{k_j}(t) \quad (10)$$

where we have suppressed the L/c-sec propagation delay and $\mathcal{F}_k$ is the unitary polarization-transformation matrix for fiber k $(k = S, I)$

$$\mathcal{F}_k\left(\theta_k,\varphi_k,\varphi'_k,\psi_k\right)=\begin{pmatrix} e^{i\psi_k}\cos\left(\frac{\theta_k}{2}\right) & -e^{i(\psi_k+\varphi_k)}\sin\left(\frac{\theta_k}{2}\right)\\ e^{i(\psi_k+\varphi'_k)}\sin\left(\frac{\theta_k}{2}\right) & e^{i(\psi_k+\varphi_k+\varphi'_k)}\cos\left(\frac{\theta_k}{2}\right)\end{pmatrix} \quad (11)$$

for $\theta_k \in [0,\pi]$ and $\varphi_k, \varphi'_k, \psi_k \in [0, 2\pi)$.

[1]Strictly speaking, we should use time-*invariant* polarization transformations, to account for the possible delay spread associated with polarization mode dispersion (PMD) [12]. Because PMD causes pulse spreading that, to first order, is independent of source bandwidth, it could pose a limiting effect on our fiber-based approach to entanglement distribution. However, recent experiments [13]—using polarization-entangled photons generated in psec-duration pairs from a nonlinear-fiber Sagnac interferometer—have successfully demonstrated entanglement transmission when the signal and idler were propagated through different 25-km-long optical fibers. Thus, we believe that PMD need not entail a serious restriction to the MIT/NU quantum communication architecture, at least over the path lengths contemplated in [1]. Moreover, by replacing the Fig. 4 setup with a more elaborate pilot-tone system that tracks one of the fiber's principal states of polarization (PSPs), instead of an arbitrary linear polarization, the effects of PMD could be further ameliorated, affording access to even longer path lengths.

The pilot pulses in each fiber, which undergo these same polarization transformations, are sufficiently strong that they behave classically, thus affording high signal-to-noise ratio measurements of $\{\theta_k, \varphi_k' : k = S, I\}$ but no information about $\{\psi_k, \varphi_k : k = S, I\}$. Polarization restoration is then performed on $\{S_1, S_2\}$ and $\{I_1, I_2\}$ using the putative inverse transformations

$$\mathcal{F}_k^{-1}\left(\tilde{\theta}_k, \tilde{\varphi}_k'\right) = \begin{pmatrix} \cos\left(\frac{\tilde{\theta}_k}{2}\right) & e^{-i\tilde{\varphi}_k'}\sin\left(\frac{\tilde{\theta}_k}{2}\right) \\ -\sin\left(\frac{\tilde{\theta}_k}{2}\right) & e^{-i\tilde{\varphi}_k'}\cos\left(\frac{\tilde{\theta}_k}{2}\right) \end{pmatrix} \quad (12)$$

where $\{\tilde{\theta}_k, \tilde{\varphi}_k' : k = S, I\}$ are estimated values derived from the pilot-pulse measurements. If these measurements are perfect, then the vector signal and idler fields *after* polarization restoration will be

$$\begin{aligned}\hat{\boldsymbol{A}}_{k_j}^{\mathrm{OUT}}(t) &= \mathcal{F}_k^{-1}\left(\theta_k, \varphi_k'\right)\mathcal{F}_k\left(\theta_k, \varphi_k, \varphi_k', \psi_k\right)\hat{\boldsymbol{A}}_{k_j}(t) \\ &= e^{i\psi_k}\left(\hat{A}_{k_j}^{\mathrm{OPA}}(t) \quad e^{i\varphi_k}\hat{A}_{k_j}^{f}(t)\right)^T \end{aligned} \quad (13)$$

hence accomplishing perfect restoration of the signal and idler time slots, up to an unimportant pair of absolute phase factors.

Errors may occur in estimating the parameters of the fiber transformations, in realizing inverse transformations based on these estimates, in extracting the x-polarized components from the polarization-restored fiber outputs, and in reassembling the polarization-entangled signal and idler fields. Collectively, these errors can all be subsumed into the following input–output transformations for lossless, imperfect polarization-restored fiber propagation:

$$\begin{aligned}\hat{\boldsymbol{A}}_S^{\mathrm{OUT}}(t) &= \begin{pmatrix}\hat{A}_{S_x}^{\mathrm{OUT}}(t) \\ \hat{A}_{S_y}^{\mathrm{OUT}}(t)\end{pmatrix} \\ &= \begin{pmatrix}\cos\left(\frac{\theta_S}{2}\right)\hat{A}_{S_1}^{\mathrm{OPA}}(t) - e^{i\varphi_S}\sin\left(\frac{\theta_S}{2}\right)\hat{A}_{S_1}^{f}(t) \\ \cos\left(\frac{\theta_S}{2}\right)\hat{A}_{S_2}^{\mathrm{OPA}}(t) - e^{i\varphi_S}\sin\left(\frac{\theta_S}{2}\right)\hat{A}_{S_2}^{f}(t)\end{pmatrix}\end{aligned} \quad (14)$$

and

$$\begin{aligned}\hat{\boldsymbol{A}}_I^{\mathrm{OUT}}(t) &= \begin{pmatrix}\hat{A}_{I_x}^{\mathrm{OUT}}(t) \\ \hat{A}_{I_y}^{\mathrm{OUT}}(t)\end{pmatrix} \\ &= \begin{pmatrix}\cos\left(\frac{\theta_I}{2}\right)\hat{A}_{I_2}^{\mathrm{OPA}}(t) - e^{i\varphi_I}\sin\left(\frac{\theta_I}{2}\right)\hat{A}_{I_2}^{f}(t) \\ \cos\left(\frac{\theta_I}{2}\right)\hat{A}_{I_1}^{\mathrm{OPA}}(t) - e^{i\varphi_I}\sin\left(\frac{\theta_I}{2}\right)\hat{A}_{I_1}^{f}(t)\end{pmatrix}\end{aligned} \quad (15)$$

where we have omitted some absolute phase factors that do not affect the cavity-loading analysis, given below, and $\{\theta_k, \varphi_k : k = S, I\}$ are now polarization-restoration *error* phases, rather than the fiber *propagation* phases appearing in (11). Because these input/output relations are linear and phase insensitive, it follows, by combining the propagation loss and imperfect polarization restoration models, that the vector output fields—which serve as inputs to the quantum memories—are in zero-mean, joint Gaussian states that are completely characterized by the following correlation functions:

$$\begin{pmatrix}K_{S_x}^{(n)}(\tau) \\ K_{S_y}^{(n)}(\tau)\end{pmatrix} = \begin{pmatrix}\left\langle \hat{A}_{S_x}^{\mathrm{OUT}\dagger}(t+\tau)\hat{A}_{S_x}^{\mathrm{OUT}}(t)\right\rangle \\ \left\langle \hat{A}_{S_y}^{\mathrm{OUT}\dagger}(t+\tau)\hat{A}_{S_y}^{\mathrm{OUT}}(t)\right\rangle\end{pmatrix} \quad (16)$$

$$= \cos^2\left(\frac{\theta_S}{2}\right)\begin{pmatrix}K_{\mathrm{OPA}_1}^{(n)}(\tau) \\ K_{\mathrm{OPA}_2}^{(n)}(\tau)\end{pmatrix} \quad (17)$$

$$\begin{pmatrix}K_{I_x}^{(n)}(\tau) \\ K_{I_y}^{(n)}(\tau)\end{pmatrix} = \begin{pmatrix}\left\langle \hat{A}_{I_x}^{\mathrm{OUT}\dagger}(t+\tau)\hat{A}_{I_x}^{\mathrm{OUT}}(t)\right\rangle \\ \left\langle \hat{A}_{I_y}^{\mathrm{OUT}\dagger}(t+\tau)\hat{A}_{I_y}^{\mathrm{OUT}}(t)\right\rangle\end{pmatrix} \quad (18)$$

$$= \cos^2\left(\frac{\theta_I}{2}\right)\begin{pmatrix}K_{\mathrm{OPA}_2}^{(n)}(\tau) \\ K_{\mathrm{OPA}_1}^{(n)}(\tau)\end{pmatrix} \quad (19)$$

and

$$\begin{pmatrix}K_{S_xI_y}^{(p)}(\tau) \\ K_{S_yI_x}^{(p)}(\tau)\end{pmatrix} = \begin{pmatrix}\left\langle \hat{A}_{S_x}^{\mathrm{OUT}}(t+\tau)\hat{A}_{I_y}^{\mathrm{OUT}}(t)\right\rangle \\ \left\langle \hat{A}_{S_y}^{\mathrm{OUT}}(t+\tau)\hat{A}_{I_x}^{\mathrm{OUT}}(t)\right\rangle\end{pmatrix} \quad (20)$$

$$= \cos\left(\frac{\theta_S}{2}\right)\cos\left(\frac{\theta_I}{2}\right)\begin{pmatrix}K_{\mathrm{OPA}_1}^{(p)}(\tau) \\ K_{\mathrm{OPA}_2}^{(p)}(\tau)\end{pmatrix}. \quad (21)$$

As expected, because OPA_1 produces entangled x-polarized signal and y-polarized idler fields and OPA_2 independently produces entangled y-polarized signal and x-polarized idler fields, these correlation functions show that the joint state (density operator) of the vector signal and idler fields arriving at the quantum memories factors according to,

$$\hat{\rho}_{\mathbf{SI}} = \hat{\rho}_{S_xI_y} \otimes \hat{\rho}_{S_yI_x}. \quad (22)$$

IV. Cavity-Loading Analysis

To derive the joint state of the quantum memories, we neglect the atom-field coupling and treat the simpler cold-cavity system, following the procedure introduced in [1]. Moreover, we will postpone accounting for dual-OPA pump detuning by assuming that $\omega_S = \omega_I = \omega_P/2 = \omega_c = \omega_a$, where ω_P is the pump frequency, ω_c is the memory-cavity resonance, and ω_a is the $^{87}\mathrm{Rb}$ atomic line.

Let $\hat{a}_S(T_c)$ and $\hat{a}_I(T_c)$ be the internal annihilation operators of the quantum memory cavities after a T_c-second long loading interval. Assume the memory cavities have input-coupling rate γ_c and cavity linewidth $\Gamma_c \geq \gamma_c$. Then, the vector (x and y) internal annihilation operators are related to the external fields by

$$\begin{aligned}\hat{\boldsymbol{a}}_k(T_c) = \hat{\boldsymbol{a}}_k(0)e^{-\Gamma_c T_c} + \int_0^{T_c} e^{-\Gamma_c(T_c - t)} \\ \times\left[\sqrt{2\gamma_c}\hat{\boldsymbol{A}}_k^{\mathrm{OUT}}(t) + \sqrt{2(\Gamma_c - \gamma_c)}\hat{\boldsymbol{A}}_k^{c}(t)\right]\mathrm{d}t\end{aligned} \quad (23)$$

for $k = S, I$, where the initial internal annihilation operators and memory-cavity loss operators $\{\hat{\boldsymbol{a}}_k(0), \hat{\boldsymbol{A}}_k^c(t)\}$ are in vacuum states. Once again we have a linear, phase-insensitive transformation, which implies that $\{\hat{\boldsymbol{a}}_S(T_c), \hat{\boldsymbol{a}}_I(T_c)\}$ are in a zero-mean joint Gaussian state. The nonzero second moments of these memory-cavity modes can be found from (17)–(21) and (23) via standard techniques. When $\Gamma_c T_c \gg 1$, as we shall assume, the results of such moment calculations are

$$\left\langle \hat{a}_{S_l}^{\dagger}(T_c)\hat{a}_{S_l}(T_c)\right\rangle = \bar{n}_{S_l}, \qquad \text{for } l = x, y \quad (24)$$

$$\left\langle \hat{a}_{I_l}^{\dagger}(T_c)\hat{a}_{I_l}(T_c)\right\rangle = \bar{n}_{I_l}, \qquad \text{for } l = x, y \quad (25)$$

$$\left\langle \hat{a}_{S_x}(T_c)\hat{a}_{I_y}(T_c)\right\rangle = \tilde{n}_{S_xI_y} \tag{26}$$

$$\left\langle \hat{a}_{S_y}(T_c)\hat{a}_{I_x}(T_c)\right\rangle = -\tilde{n}_{S_yI_x} \tag{27}$$

with

$$\bar{n}_{S_x} = \cos^2\left(\frac{\theta_S}{2}\right)\left(|I_{1-}| - |I_{1+}|\right) \tag{28}$$

$$\bar{n}_{S_y} = \cos^2\left(\frac{\theta_S}{2}\right)\left(|I_{2-}| - |I_{2+}|\right) \tag{29}$$

$$\bar{n}_{I_x} = \cos^2\left(\frac{\theta_I}{2}\right)\left(|I_{2-}| - |I_{2+}|\right) \tag{30}$$

$$\bar{n}_{I_y} = \cos^2\left(\frac{\theta_I}{2}\right)\left(|I_{1-}| - |I_{1+}|\right) \tag{31}$$

$$\tilde{n}_{S_xI_y} = \cos\left(\frac{\theta_S}{2}\right)\cos\left(\frac{\theta_I}{2}\right)\left(I_{1-} + I_{1+}\right) \tag{32}$$

$$\tilde{n}_{S_yI_x} = \cos\left(\frac{\theta_S}{2}\right)\cos\left(\frac{\theta_I}{2}\right)\left(I_{2-} + I_{2+}\right) \tag{33}$$

and

$$I_{j\pm} = \frac{\eta_L\gamma\gamma_c}{\Gamma\Gamma_c}\frac{G_j}{\left(1 \pm |G_j|\right)\left(1 \pm |G_j| + \frac{\Gamma_c}{\Gamma}\right)} \tag{34}$$

for $j = 1, 2$. In terms of these moments, we have that the joint antinormally-ordered characteristic function for the $\{\hat{\boldsymbol{a}}_S(T_c), \hat{\boldsymbol{a}}_I(T_c)\}$ modes is the Gaussian form

$$\begin{aligned}\chi_A\left(\zeta_{S_x}, \zeta_{S_y}, \zeta_{I_x}, \zeta_{I_y}\right) &= \exp\Big[-\left(1+\bar{n}_{S_x}\right)|\zeta_{S_x}|^2 \\ &\quad - \left(1+\bar{n}_{S_y}\right)\left|\zeta_{S_y}\right|^2 \\ &\quad - \left(1+\bar{n}_{I_x}\right)|\zeta_{I_x}|^2 \\ &\quad - \left(1+\bar{n}_{I_y}\right)\left|\zeta_{I_y}\right|^2 \\ &\quad + 2\mathrm{Re}\left(\tilde{n}^*_{S_xI_y}\zeta_{S_x}\zeta_{I_y}\right) \\ &\quad - 2\mathrm{Re}\left(\tilde{n}^*_{S_yI_x}\zeta_{S_y}\zeta_{I_x}\right)\Big].\end{aligned} \tag{35}$$

V. Single-Photon Error Model

The cold-cavity loading analysis includes the possibility that more than one photon may be loaded into either memory, yet this is clearly not possible for the actual trapped-atom memory. As a result, the initial assessment of throughput versus fidelity, reported in [1], treated the loading of a singlet state into the two memories as a *success*, and any other event in which one or more photons were loaded into each memory as an *error*. Load intervals in which one or both of the memories fail to absorb a photon were considered to be *erasures*, because they could be detected, nondestructively, by means of the A-to-C cycling transition shown in Fig. 2(a), see [1] and [4] for details. Erasures reduce teleportation throughput in the Fig. 1 architecture, but not its fidelity. A better approximation to performance analysis for the Fig. 1 architecture was presented in [14] (see also [15]), where multiple-atom arrays at each memory location were used to convert multi-photon error events from [1] into erasures. Both the analysis in [1] and that in [14] assume amplitude matched, anti-phased pumping in the dual-OPA source, viz., $G_1 = G_2 = G$, and perfect polarization restoration, i.e., $\theta_S = \theta_I = 0$. Our task, in this section, is to generalize the single-photon error model of [14] to include amplitude and phase errors in the dual-OPAs pumps as well as imperfect polarization restoration. The results we obtain here will then enable us to evaluate the impact these effects have on the teleportation throughput and fidelity.

Define the computational basis of the quantum memories to be $|0\rangle_k = |10\rangle_{k_xk_y}$ and $|1\rangle_k = |01\rangle_{k_xk_y}$, for $k = S, I$, where $|10\rangle_{S_xS_y}$ denotes the memory state generated by absorption of an x-polarized signal photon, etc. To compute the entries of the conditional density matrix for the memories, given that each has absorbed a single photon, we first write the density operators $\hat{\rho}_{S_xI_y}$ and $\hat{\rho}_{S_yI_x}$ in terms of their respective antinormally-ordered characteristic functions via the operator-valued inverse Fourier transform relations

$$\begin{aligned}\hat{\rho}_{S_xI_y} = \int\frac{\mathrm{d}^2\zeta_S}{\pi}\int\frac{\mathrm{d}^2\zeta_I}{\pi}\chi_A^{\rho_{S_xI_y}}(\zeta_S,\zeta_I) \\ \times\, e^{-\zeta_S\hat{a}^\dagger_{S_x} - \zeta_I\hat{a}^\dagger_{I_y}}e^{\zeta_S^*\hat{a}_{S_x} + \zeta_I^*\hat{a}_{I_y}}\end{aligned} \tag{36}$$

and

$$\begin{aligned}\hat{\rho}_{S_yI_x} = \int\frac{\mathrm{d}^2\zeta_S}{\pi}\int\frac{\mathrm{d}^2\zeta_I}{\pi}\chi_A^{\rho_{S_yI_x}}(\zeta_S,\zeta_I) \\ \times\, e^{-\zeta_S\hat{a}^\dagger_{S_y} - \zeta_I\hat{a}^\dagger_{I_x}}e^{\zeta_S^*\hat{a}_{S_y} + \zeta_I^*\hat{a}_{I_x}}\end{aligned} \tag{37}$$

where, for the sake of brevity, we have suppressed the T_c time argument of the cavity-mode annihilation operators. The characteristic function associated with $\hat{\rho}_{S_xI_y}$ can be expressed as

$$\chi_A^{\rho_{S_xI_y}}(\boldsymbol{\zeta}) = \frac{\pi^2 p_{S_xI_y}(\boldsymbol{\zeta})}{D_1} \tag{38}$$

where $D_1 = (1+\bar{n}_{S_x})(1+\bar{n}_{I_y}) - |\tilde{n}_{S_xI_y}|^2$ and $p_{S_xI_y}(\boldsymbol{\zeta})$ is the classical probability density of a zero-mean, complex-valued Gaussian random vector $\boldsymbol{\zeta} = (\zeta_S\ \zeta_I)^T$ with second-moment matrices

$$\langle\boldsymbol{\zeta}\boldsymbol{\zeta}^\dagger\rangle_{p_{S_xI_y}} = \frac{1}{D_1}\begin{pmatrix}1+\bar{n}_{I_y} & 0\\ 0 & 1+\bar{n}_{S_x}\end{pmatrix} \tag{39}$$

$$\langle\boldsymbol{\zeta}\boldsymbol{\zeta}^T\rangle_{p_{S_xI_y}} = \frac{1}{D_1}\begin{pmatrix}0 & \tilde{n}_{S_xI_y}\\ \tilde{n}_{S_xI_y} & 0\end{pmatrix}. \tag{40}$$

Similarly, we have

$$\chi_A^{\rho_{S_yI_x}}(\boldsymbol{\zeta}) = \frac{\pi^2 p_{S_yI_x}(\boldsymbol{\zeta})}{D_2} \tag{41}$$

where $D_2 = (1+\bar{n}_{S_y})(1+\bar{n}_{I_x}) - |\tilde{n}_{S_yI_x}|^2$ and $p_{S_yI_x}(\boldsymbol{\zeta})$ is the classical probability density of a zero-mean, complex-valued Gaussian random vector $\boldsymbol{\zeta} = (\zeta_S\ \zeta_I)^T$ with second-moment matrices

$$\langle\boldsymbol{\zeta}\boldsymbol{\zeta}^\dagger\rangle_{p_{S_yI_x}} = \frac{1}{D_2}\begin{pmatrix}1+\bar{n}_{I_x} & 0\\ 0 & 1+\bar{n}_{S_y}\end{pmatrix} \tag{42}$$

$$\langle\boldsymbol{\zeta}\boldsymbol{\zeta}^T\rangle_{p_{S_yI_x}} = \frac{1}{D_2}\begin{pmatrix}0 & -\tilde{n}_{S_yI_x}\\ -\tilde{n}_{S_yI_x} & 0\end{pmatrix}. \tag{43}$$

The conditional single-photon density matrix will be computed in the standard basis, $\{|00\rangle_{SI}, |01\rangle_{SI}, |10\rangle_{SI}, |11\rangle_{SI}\}$. Define the quantities

$$N_{S_x} = \bar{n}_{S_x}\left(1+\bar{n}_{I_y}\right) - \left|\tilde{n}_{S_xI_y}\right|^2 \quad (44)$$
$$N_{S_y} = \bar{n}_{S_y}\left(1+\bar{n}_{I_x}\right) - \left|\tilde{n}_{S_yI_x}\right|^2 \quad (45)$$
$$N_{I_x} = \bar{n}_{I_x}\left(1+\bar{n}_{S_y}\right) - \left|\tilde{n}_{S_yI_x}\right|^2 \quad (46)$$
$$N_{I_y} = \bar{n}_{I_y}\left(1+\bar{n}_{S_x}\right) - \left|\tilde{n}_{S_xI_y}\right|^2. \quad (47)$$

Then, the ten density matrix entries we need to compute are

$$\begin{aligned}
{}_{SI}\langle 00|\hat{\rho}_{\mathbf{SI}}|00\rangle_{SI} &= \left\langle 10\left|\hat{\rho}_{S_xI_y}\right|10\right\rangle\left\langle 01\left|\hat{\rho}_{S_yI_x}\right|01\right\rangle && (48)\\
&= \frac{\left\langle 1-|\zeta_S|^2\right\rangle_{p_{SxIy}}\left\langle 1-|\zeta_I|^2\right\rangle_{p_{SyIx}}}{D_1D_2} && (49)\\
&= \frac{N_{S_x}N_{I_x}}{D_1^2D_2^2} && (50)\\
{}_{SI}\langle 00|\hat{\rho}_{\mathbf{SI}}|01\rangle_{SI} &= \left\langle 10\left|\hat{\rho}_{S_xI_y}\right|11\right\rangle\left\langle 01\left|\hat{\rho}_{S_yI_x}\right|00\right\rangle && (51)\\
&= \frac{\left\langle\left(1-|\zeta_S|^2\right)\zeta_I^*\right\rangle_{p_{SxIy}}\left\langle-\zeta_I\right\rangle_{p_{SyIx}}}{D_1D_2} && (52)\\
&= 0 && (53)\\
{}_{SI}\langle 00|\hat{\rho}_{\mathbf{SI}}|10\rangle_{SI} &= \left\langle 10\left|\hat{\rho}_{S_xI_y}\right|00\right\rangle\left\langle 01\left|\hat{\rho}_{S_yI_x}\right|11\right\rangle && (54)\\
&= \frac{\left\langle-\zeta_S\right\rangle_{p_{SxIy}}\left\langle\zeta_S^*\left(1-|\zeta_I|^2\right)\right\rangle_{p_{SyIx}}}{D_1D_2} && (55)\\
&= 0 && (56)\\
{}_{SI}\langle 00|\hat{\rho}_{\mathbf{SI}}|11\rangle_{SI} &= \left\langle 10\left|\hat{\rho}_{S_xI_y}\right|01\right\rangle\left\langle 01\left|\hat{\rho}_{S_yI_x}\right|10\right\rangle && (57)\\
&= \frac{\left\langle-\zeta_S\zeta_I^*\right\rangle_{p_{SxIy}}\left\langle-\zeta_S^*\zeta_I\right\rangle_{p_{SyIx}}}{D_1D_2} && (58)\\
&= 0 && (59)\\
{}_{SI}\langle 01|\hat{\rho}_{\mathbf{SI}}|01\rangle_{SI} &= \left\langle 11\left|\hat{\rho}_{S_xI_y}\right|11\right\rangle\left\langle 00\left|\hat{\rho}_{S_yI_x}\right|00\right\rangle && (60)\\
&= \frac{\left\langle\left(1-|\zeta_S|^2\right)\left(1-|\zeta_I|^2\right)\right\rangle_{p_{SxIy}}}{D_1D_2} && (61)\\
&= \frac{N_{S_x}N_{I_y}+\left|\tilde{n}_{S_xI_y}\right|^2}{D_1^3D_2} && (62)\\
{}_{SI}\langle 01|\hat{\rho}_{\mathbf{SI}}|10\rangle_{SI} &= \left\langle 11\left|\hat{\rho}_{S_xI_y}\right|00\right\rangle\left\langle 00\left|\hat{\rho}_{S_yI_x}\right|11\right\rangle && (63)\\
&= \frac{\left\langle\zeta_S\zeta_I\right\rangle_{p_{SxIy}}\left\langle\zeta_S^*\zeta_I^*\right\rangle_{p_{SyIx}}}{D_1D_2} && (64)\\
&= -\frac{\tilde{n}_{S_xI_y}\tilde{n}^*_{S_yI_x}}{D_1^2D_2^2} && (65)\\
{}_{SI}\langle 01|\hat{\rho}_{\mathbf{SI}}|11\rangle_{SI} &= \left\langle 11\left|\hat{\rho}_{S_xI_y}\right|01\right\rangle\left\langle 00\left|\hat{\rho}_{S_yI_x}\right|10\right\rangle && (66)\\
&= \frac{\left\langle-\zeta_S\left(1-|\zeta_I|^2\right)\right\rangle_{p_{SxIy}}\left\langle\zeta_S^*\right\rangle_{p_{SyIx}}}{D_1D_2} && (67)\\
&= 0 && (68)\\
{}_{SI}\langle 10|\hat{\rho}_{\mathbf{SI}}|10\rangle_{SI} &= \left\langle 00\left|\hat{\rho}_{S_xI_y}\right|00\right\rangle\left\langle 11\left|\hat{\rho}_{S_yI_x}\right|11\right\rangle && (69)\\
&= \frac{\left\langle\left(1-|\zeta_S|^2\right)\left(1-|\zeta_I|^2\right)\right\rangle_{p_{SyIx}}}{D_1D_2} && (70)\\
&= \frac{N_{I_x}N_{S_y}+\left|\tilde{n}_{S_yI_x}\right|^2}{D_1D_2^3} && (71)\\
{}_{SI}\langle 10|\hat{\rho}_{\mathbf{SI}}|11\rangle_{SI} &= \left\langle 00\left|\hat{\rho}_{S_xI_y}\right|01\right\rangle\left\langle 11\left|\hat{\rho}_{S_yI_x}\right|10\right\rangle && (72)\\
&= \frac{\left\langle\zeta_I^*\right\rangle_{p_{SxIy}}\left\langle-\left(1-|\zeta_S|^2\right)\zeta_I\right\rangle_{p_{SyIx}}}{D_1D_2} && (73)\\
&= 0 && (74)\\
{}_{SI}\langle 11|\hat{\rho}_{\mathbf{SI}}|11\rangle_{SI} &= \left\langle 01\left|\hat{\rho}_{S_xI_y}\right|01\right\rangle\left\langle 10\left|\hat{\rho}_{S_yI_x}\right|10\right\rangle && (75)\\
&= \frac{\left\langle 1-|\zeta_I|^2\right\rangle_{p_{SxIy}}\left\langle 1-|\zeta_S|^2\right\rangle_{p_{SyIx}}}{D_1D_2} && (76)\\
&= \frac{N_{S_y}N_{I_y}}{D_1^2D_2^2}. && (77)
\end{aligned}$$

The right-hand side of the first equality in all these density matrix evaluations has broken the calculational basis into its constituent $\{S_x, I_y\}$ and $\{S_y, I_x\}$ photon-state components. Equations (62) and (71) were obtained via the Gaussian moment-factoring theorem.

The conditional single-photon density matrix resulting from the Gaussian state (35) in the standard basis, for fixed values of the dual-OPA pump and fiber polarization-restoration parameters, is the trace-normalized version of the preceding matrix elements

$$\hat{\rho} = \begin{pmatrix} a_1 & 0 & 0 & 0\\ 0 & b_1 & c & 0\\ 0 & c^* & b_2 & 0\\ 0 & 0 & 0 & a_2 \end{pmatrix} \quad (78)$$

where

$$a_1 = \frac{N_{S_x}N_{I_x}D_1D_2}{D'} \quad (79)$$
$$a_2 = \frac{N_{S_y}N_{I_y}D_1D_2}{D'} \quad (80)$$
$$b_1 = \frac{\left(N_{S_x}N_{I_y}+\left|\tilde{n}_{S_xI_y}\right|^2\right)D_2^2}{D'} \quad (81)$$
$$b_2 = \frac{\left(N_{S_y}N_{I_x}+\left|\tilde{n}_{S_yI_x}\right|^2\right)D_1^2}{D'} \quad (82)$$
$$c = -\frac{\tilde{n}_{S_xI_y}\tilde{n}^*_{S_yI_x}D_1D_2}{D'} \quad (83)$$

and

$$\begin{aligned}
D' = &\left(N_{S_x}N_{I_x}+N_{S_y}N_{I_y}\right)D_1D_2\\
&+\left(N_{S_x}N_{I_y}+\left|\tilde{n}_{S_xI_y}\right|^2\right)D_2^2\\
&+\left(N_{S_y}N_{I_x}+\left|\tilde{n}_{S_yI_x}\right|^2\right)D_1^2. \quad (84)
\end{aligned}$$

The single-photon density matrix $\hat{\rho}$ depends on the normalized pump magnitudes, $\{|G_1|, |G_2|\}$, the differential-phase error between the pumps, $\Delta\psi = \arg(G_1) - \arg(G_2)$, and the polarization-restoration error angles $\{\theta_S, \theta_I\}$. Note that, in general, $\hat{\rho}$ is not a Bell-diagonal state. We can apply a change of basis to show that the density matrix in the Bell basis, $\{|\psi^-\rangle_{SI}, |\psi^+\rangle_{SI}, |\phi^-\rangle_{SI}, |\phi^+\rangle_{SI}\}$, is 2×2 block diagonal, viz.

$$\hat{\rho} = \begin{pmatrix} \rho_{11} & \mathbf{0}\\ \mathbf{0} & \rho_{22} \end{pmatrix} \quad (85)$$

where

$$\rho_{11} = \frac{1}{2}\begin{pmatrix} b_1 + b_2 - 2\mathrm{Re}(c) & b_1 - b_2 + 2i\mathrm{Im}(c) \\ b_1 - b_2 - 2i\mathrm{Im}(c) & b_1 + b_2 + 2\mathrm{Re}(c) \end{pmatrix} \quad (86)$$

and

$$\rho_{22} = \frac{1}{2}\begin{pmatrix} a_1 + a_2 & a_1 - a_2 \\ a_1 - a_2 & a_1 + a_2 \end{pmatrix}. \quad (87)$$

It will be useful to know the eigendecomposition of the single-photon density matrix $\hat{\rho}$ for the performance analysis in the next section. The eigenvalues of $\hat{\rho}$ are $\{a_1, a_2, \lambda^+, \lambda^-\}$ with corresponding unit-length eigenkets $\{|00\rangle_{SI}, |11\rangle_{SI}, |\lambda^+\rangle_{SI}, |\lambda^-\rangle_{SI}\}$, where

$$\lambda^{\pm} = \frac{b_1 + b_2}{2} \pm \frac{1}{2}\sqrt{(b_1 - b_2)^2 + 4|c|^2} \quad (88)$$

$$|\lambda^+\rangle_{SI} = u_1|01\rangle_{SI} + u_2|10\rangle_{SI} \quad (89)$$

$$|\lambda^-\rangle_{SI} = v_1|01\rangle_{SI} + v_2|10\rangle_{SI}. \quad (90)$$

The eigenket coefficients u_1, u_2, v_1, v_2 are found by converting the following unnormalized eigenkets to unit length:

$$|\lambda^{\pm}\rangle_{SI} = \frac{b_1 - b_2 \pm \sqrt{(b_1 - b_2)^2 + 4|c|^2}}{2c^*}|01\rangle_{SI} + |10\rangle_{SI}. \quad (91)$$

VI. Performance Analysis

In this section, we will examine the effects of system errors on the average fidelity of the Fig. 1 teleportation architecture. We shall also give some consideration to the achievable throughput that can be obtained when each quantum memory is capable of loading a succession of singlet states by repeated application of the memory-loading protocol, cf. [1] and [14].

A. Teleportation Fidelity

Suppose the qubit that we wish to teleport is $|\phi\rangle = \alpha|0\rangle + \beta|1\rangle$. If the received state that results from sending this state via the Fig. 1 teleportation system is $\hat{\rho}'$, then the *conditional* fidelity, given that $|\phi\rangle$ was teleported, is $\langle\phi|\hat{\rho}'|\phi\rangle$. The *average* fidelity is obtained by taking $|\phi\rangle$ to be uniformly distributed over the Bloch sphere and averaging the conditional fidelity using this input distribution. We will calculate the average fidelity in the single-photon error model developed in Section V. To do so, we first calculate four pure-state average fidelities: the average fidelities realized when the quantum memories are in one of the eigenkets of the single-photon-error density matrix, $\{|00\rangle_{SI}, |11\rangle_{SI}, |\lambda^+\rangle_{SI}, |\lambda^-\rangle_{SI}\}$. Multiplying each eigenket's fidelity by its associated eigenvalue and summing the results then yields the average fidelity for the single-photon-error density matrix, $\hat{\rho}$.

Teleportation when the quantum memories are in either the $|00\rangle_{SI}$ or $|11\rangle_{SI}$ states is equivalent to a channel that sends an input qubit $|\phi\rangle = \alpha|0\rangle + \beta|1\rangle$ into the mixed state $|\beta|^2|0\rangle\langle 0| + |\alpha|^2|1\rangle\langle 1|$, and hence a conditional fidelity of $2|\alpha|^2|\beta|^2$. Averaging this expression over the Bloch sphere yields fidelity $F = 1/3$.

Teleportation when the quantum memories are in the $|\lambda^+\rangle_{SI} = u_1|01\rangle_{SI} + u_2|10\rangle_{SI}$ state takes the input qubit to the mixed state

$$|\alpha|^2|0\rangle\langle 0| + |\beta|^2|1\rangle\langle 1| - 2\alpha\beta^*\mathrm{Re}\left(u_1^* u_2\right)|0\rangle\langle 1| - 2\alpha^*\beta\mathrm{Re}\left(u_1^* u_2\right)|1\rangle\langle 0| \quad (92)$$

and, hence, a conditional fidelity $1 - 2|\alpha|^2|\beta|^2[1 + 2\mathrm{Re}(u_1^* u_2)]$. Averaging this expression over the Bloch sphere yields fidelity $F = 2[1 - \mathrm{Re}(u_1^* u_2)]/3$. Similarly, teleportation when the quantum memories are in the $|\lambda^-\rangle_{SI} = v_1|01\rangle_{SI} + v_2|10\rangle_{SI}$ state has average fidelity $F = 2[1 - \mathrm{Re}(v_1^* v_2)]/3$.

Performing the required eigenvalue weighting and summation on the preceding pure-state fidelities we obtain the average fidelity for the single-photon-error model's density matrix:

$$F = \frac{2 - a_1 - a_2 - 2\left[\lambda^+\mathrm{Re}\left(u_1^* u_2\right) + \lambda^-\mathrm{Re}(v_1^* v_2)\right]}{3}. \quad (93)$$

This is the average teleportation fidelity, with the input qubit $\alpha|0\rangle + \beta|1\rangle$ uniformly distributed over the Bloch sphere, for fixed values of the error parameters.

To develop insight into how teleportation performance is degraded by errors in the dual-OPAs pump amplitudes and phases as well as by imperfect polarization restoration, we shall examine these effects one at a time.

B. Imperfect Polarization Restoration

Here we assume the dual-OPAs pumps have equal magnitudes, $|G_1| = |G_2| = |G|$, and are anti-phased, $\Delta\psi = 0$. In this case, the single-photon-error density matrix is diagonal in the Bell basis, and given by

$$\hat{\rho} = \mathrm{diag}\begin{pmatrix} P_s & \frac{P_e}{3} & \frac{P_e}{3} & \frac{P_e}{3} \end{pmatrix} \quad (94)$$

where P_s is the success probability and $P_e = 1 - P_s$ is the error probability,[2] and

$$P_s = \frac{N_S N_I + 2\tilde{n}^2}{4N_S N_I + 2\tilde{n}^2} \tag{95}$$

$$N_S = \bar{n}_S(1 + \bar{n}_I) - \tilde{n}^2 \tag{96}$$

$$N_I = \bar{n}_I(1 + \bar{n}_S) - \tilde{n}^2 \tag{97}$$

$$\bar{n}_S = \cos^2\left(\frac{\theta_S}{2}\right)(I_- - I_+) \tag{98}$$

$$\bar{n}_I = \cos^2\left(\frac{\theta_I}{2}\right)(I_- - I_+) \tag{99}$$

$$\tilde{n} = \cos\left(\frac{\theta_S}{2}\right)\cos\left(\frac{\theta_I}{2}\right)(I_- + I_+) \tag{100}$$

$$I_\pm = \frac{\eta_L \gamma \gamma_c}{\Gamma \Gamma_c} \frac{|G|}{(1 \pm |G|)\left(1 \pm |G| + \frac{\Gamma_c}{\Gamma}\right)}. \tag{101}$$

The density matrix (94) is a Werner state, so teleporting a qubit with this state is equivalent to transmitting the qubit over a depolarizing channel with fidelity P_s. The average teleportation fidelity with this error model is $F = (2P_s + 1)/3$.

In Fig. 6, the teleportation fidelity is plotted versus the polarization-restoration error parameters θ_S, $\theta_I \in [0, \pi]$. The calculations assume a source-to-memory path length $L = 25$ km and the operating conditions listed in the caption. The performance of the teleportation system is insensitive to θ_S and θ_I. Maximum fidelity, $F = 0.978$, occurs at $\theta_S = \theta_I = 0$, and minimum fidelity, $F = 0.974$, occurs at $\theta_S = \theta_I = \pi$.

Although teleportation fidelity is insensitive to imperfect polarization restoration, these errors imply a significant loss of singlet-state throughput, i.e., the number of singlets/sec that could be stored by repeated application of the loading protocol at rate R using a bank of trapped-atom quantum memories [1].[3] Fig. 7 plots the throughput versus θ_S, $\theta_I \in [0, \pi]$, assuming that the loading protocol is run at $R = 500$ kHz. The other parameters for this figure are the same as those for Fig. 6. We see from Fig. 7 that maximum throughput at $L = 25$ km is approximately 184 singlets/s and this occurs when the polarization restoration is perfect, $\theta_S = \theta_I = 0$. The throughput decreases to zero when θ_S or θ_I approaches π rad. In essence, $\cos(\theta_S/2)$ and $\cos(\theta_I/2)$ act as asymmetric loss factors on the signal and idler fiber channels, respectively. For small values of θ_S and θ_I it is possible to obtain a simple analytic expression for the success probability, P_s, by means of a Taylor series expansion; we find that

$$P_S \approx \frac{N_0^2 + 2\tilde{n}_0^2}{4N_0^2 + 2\tilde{n}_0^2} - \frac{3N_0\tilde{n}_0^2\left(\tilde{n}_0^2 - \bar{n}_0^2\right)}{8\left(2N_0^2 + \tilde{n}_0^2\right)^2}\left(\theta_S^2 + \theta_I^2\right) \tag{102}$$

where $N_0 = \bar{n}_0(1 + \bar{n}_0) - \tilde{n}_0^2$ with $\bar{n}_0 = I_- - I_+$ and $\tilde{n}_0 = I_- + I_+$. Thus, to lowest order, the throughput of the Fig. 1 teleportation system degrades with the sum of the squares of the polarization-restoration errors θ_S and θ_I.

[2]The success event was defined in [1] to be the loading of a singlet state into the two memories. Thus, strictly speaking, P_s is the conditional probability of a success event, given that an erasure has not occurred. Likewise, P_e is the conditional probability of a single-photon error event given there has not been an erasure.

[3]Throughput equals ${}_{SI}\langle\psi^-|\hat{\rho}_{\mathbf{SI}}|\psi^-\rangle_{SI} R$, i.e., the *unconditional* probability that a singlet state is loaded times the memory cycling rate.

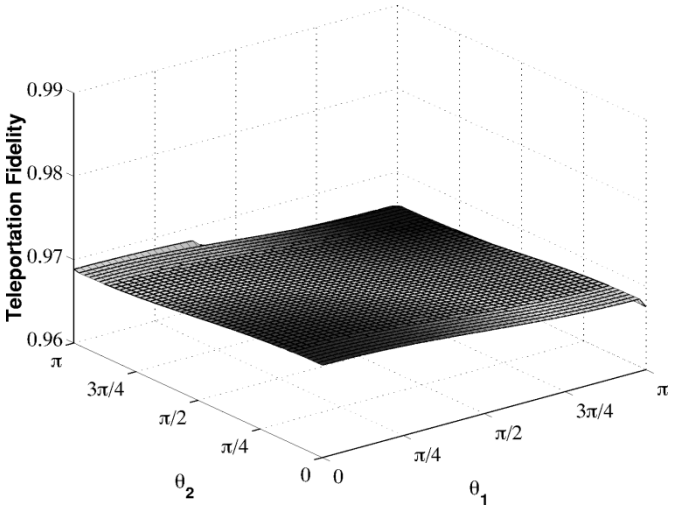

Fig. 6. Teleportation fidelity versus polarization-restoration error parameters θ_S, $\theta_I \in [0, \pi]$. We assume the OPAs operate at 1% of oscillation threshold, 0.2-dB/km fiber loss, 5-dB excess loss in each source-to-memory link, $\Gamma_c/\Gamma = 0.5$ memory-cavity linewidth to source-cavity linewidth ratio, and source-to-memory path length $L = 25$ km.

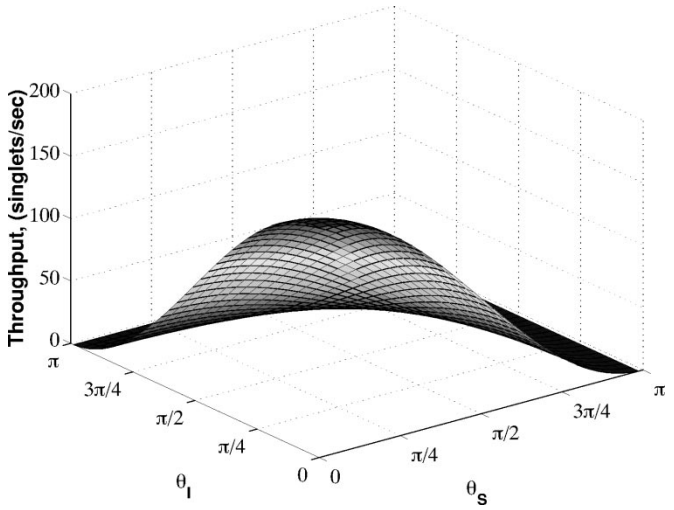

Fig. 7. Throughput of singlet states versus polarization-restoration error parameters θ_S, $\theta_I \in [0, \pi]$. We assume the loading protocol operates at a 500-kHz cycling rate. The other parameters for this plot are the same as those for Fig. 6.

C. OPA Pump-Phase Error

Here, we assume $|G_1| = |G_2| = |G|$ and $\theta_S = \theta_I = 0$, and consider the impact of a pump-phase error, i.e., of having $\Delta\psi = \arg(G_1) - \arg(G_2) \neq 0$. In this case, the single-photon-error density matrix in the Bell basis is

$$\hat{\rho} = \begin{pmatrix} b - \mathrm{Re}(c) & i\mathrm{Im}(c) & 0 & 0 \\ -i\mathrm{Im}(c) & b + \mathrm{Re}(c) & 0 & 0 \\ 0 & 0 & a & 0 \\ 0 & 0 & 0 & a \end{pmatrix} \tag{103}$$

where

$$a = \frac{N^2}{4N^2 + 2\tilde{n}^2} \tag{104}$$

$$b = \frac{N^2 + \tilde{n}^2}{4N^2 + 2\tilde{n}^2} \tag{105}$$

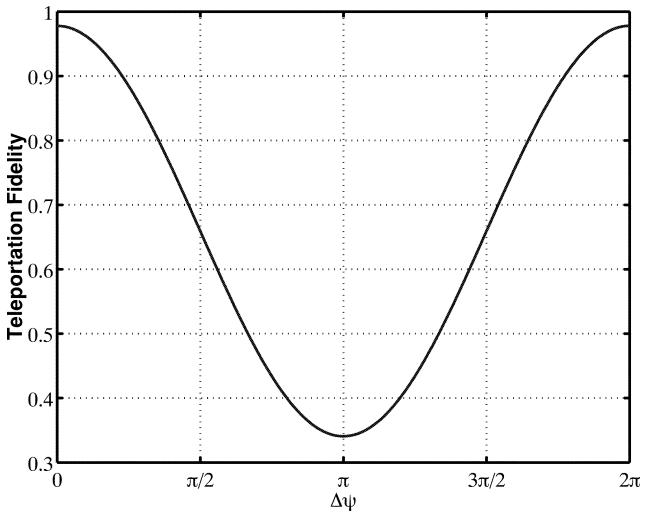

Fig. 8. Teleportation fidelity versus dual-OPA pump-phase error $\Delta\psi \in [0, 2\pi)$. At $\Delta\psi = \pi$, the dominant eigenket of $\hat{\rho}$ is the triplet state, so the teleportation fidelity is approximately 1/3. We assume the same operating conditions as in Fig. 6.

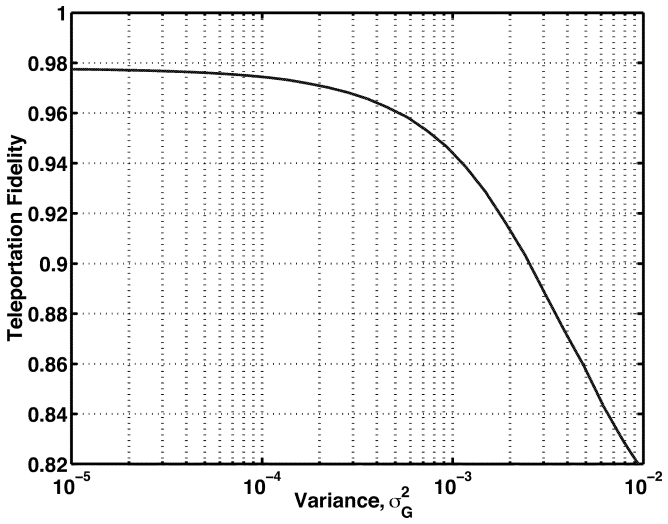

Fig. 9. Teleportation fidelity versus the variance of OPA pump-amplitude fluctuations. G_1 and G_2 are taken to be statistically independent, identically distributed, real-valued Gaussian random variables with means 0.1 and variances σ_G^2. We assume the same operating conditions as in Fig. 6.

$$c = -\frac{e^{i\Delta\psi}\tilde{n}^2}{4N^2 + 2\tilde{n}^2} \tag{106}$$

$$N = \bar{n}(1+\bar{n}) - \tilde{n}^2 \tag{107}$$

$$\bar{n} = I_- - I_+ \tag{108}$$

$$\tilde{n} = I_- + I_+ \tag{109}$$

$$I_\pm = \frac{\eta_L\gamma\gamma_c}{\Gamma\Gamma_c}\frac{|G|}{(1\pm|G|)\left(1\pm|G|+\frac{\Gamma_c}{\Gamma}\right)}. \tag{110}$$

The density matrix is not Bell-diagonal. Its eigenkets are $\{|00\rangle_{SI}, |11\rangle_{SI}, |\lambda^+\rangle_{SI}, |\lambda^-\rangle_{SI}\}$, where

$$|\lambda^\pm\rangle_{SI} = \frac{1}{\sqrt{2}}\left(|01\rangle_{SI} \mp e^{-i\Delta\psi}|10\rangle_{SI}\right). \tag{111}$$

From (88), the eigenvalues associated with $|\lambda^\pm\rangle_{SI}$ are $\lambda^\pm = b \pm |c|$. From the expressions above we see that $\lambda^- = a$. Substituting the values $u_1 = v_1 = 1/\sqrt{2}$, $-u_2 = v_2 = e^{-i\Delta\psi}/\sqrt{2}$, and $\lambda^+ = 1 - 3a$ into the (93) gives the average teleportation fidelity

$$F = \frac{2 - 2a + (1-4a)\cos\Delta\psi}{3}. \tag{112}$$

We have plotted the fidelity from (112) versus the pump-phase error $\Delta\psi$ in Fig. 8, assuming $L = 25$ km source-to-memory path length and the same operating conditions as in Fig. 6. Fig. 8 shows that pump-phase errors have serious consequences: at $\Delta\psi = \pi$, the dominant eigenket $|\lambda^+\rangle_{SI}$ equals the triplet state, making the average fidelity close to the triplet-state value, $F = 1/3$. For small values of the pump-phase error, we can use a Taylor-series expansion to show that

$$F \approx F_0 - \frac{(1-4a)\Delta\psi^2}{6} \tag{113}$$

where F_0 is the average fidelity for antiphased pumps, i.e., when $\Delta\psi = 0$.

D. OPA Pump-Amplitude Fluctuations

Now, we will study the effects of OPA pump-amplitude fluctuations—G_1 and G_2 will be taken to be statistically independent, identically distributed, real-valued Gaussian random variables with mean values 0.1 and variances σ_G^2—when the polarization restoration is perfect ($\theta_S = \theta_I = 0$). In this case, the single-photon-error density matrix, given $\{G_1, G_2\}$, is

$$\hat{\rho} = \begin{pmatrix} \frac{1}{2}(b_1+b_2) - c & \frac{1}{2}(b_1-b_2) & 0 & 0 \\ \frac{1}{2}(b_1-b_2) & \frac{1}{2}(b_1+b_2) + c & 0 & 0 \\ 0 & 0 & a & 0 \\ 0 & 0 & 0 & a \end{pmatrix} \tag{114}$$

in the Bell basis, where, for $j = 1, 2$

$$a = \frac{N_1 N_2 D_1 D_2}{D'} \tag{115}$$

$$b_1 = \frac{\left(N_1^2 + \tilde{n}_1^2\right) D_2^2}{D'} \tag{116}$$

$$b_2 = \frac{\left(N_2^2 + \tilde{n}_2^2\right) D_1^2}{D'} \tag{117}$$

$$c = -\frac{\tilde{n}_1\tilde{n}_2 D_1 D_2}{D'} \tag{118}$$

$$N_j = \bar{n}_j(1+\bar{n}_j) - \tilde{n}_j^2 \tag{119}$$

$$D_j = (1+\bar{n}_j)^2 - \tilde{n}_j^2 \tag{120}$$

$$D' = 2N_1N_2D_1D_2 + \left(N_1^2 + \tilde{n}_1^2\right) D_2^2 + \left(N_2^2 + \tilde{n}_2^2\right) D_1^2 \tag{121}$$

$$\bar{n}_j = I_{j-} - I_{j+} \tag{122}$$

$$\tilde{n}_j = I_{j-} + I_{j+} \tag{123}$$

$$I_{j\pm} = \frac{\eta_L\gamma\gamma_c}{\Gamma\Gamma_c}\frac{G_j}{(1\pm G_j)\left(1\pm G_j + \frac{\Gamma_c}{\Gamma}\right)}. \tag{124}$$

Fig. 9 shows simulation results for the average teleportation fidelity in the presence of these pump-amplitude fluctuations. The calculations assume an $L = 25$ km source-to-memory path length and same operating conditions as in Fig. 6. We see

from this figure that pump-amplitude fluctuations should not be problematic: For 1% pump-power fluctuations with a mean pump power that is ~1% of oscillation threshold we have that $\sigma_G^2 \sim 10^{-4}$.

E. Detuning

At this juncture we turn to the effects of pump frequency errors. Suppose that the pumps have equal amplitudes and are antiphased with $G_1 = G_2 = G > 0$, and that the polarization restoration is perfect. So far we have assumed that the dual-OPAs signal and idler frequencies are equal and equal to both the memory cavities' resonance frequency and the $^{87}\mathrm{Rb}$ atomic line, i.e., $\omega_S = \omega_I = \omega_c = \omega_a$. In this final assessment of teleportation system errors, we shall consider two possible cases of frequency detuning. In case 1, we shall assume that the dual-OPA operates somewhat off frequency degeneracy, so that the signal and idler frequencies are $\omega_S = \omega_P/2 + \Delta\omega$ and $\omega_I = \omega_P/2 - \Delta\omega$, with the frequency degeneracy point satisfying, $\omega_P/2 = \omega_c = \omega_a$, i.e., matched to the memory cavity and the $^{87}\mathrm{Rb}$ atomic line. In case 2 the dual-OPA operates at frequency degeneracy, $\omega_S = \omega_I = \omega_P/2$, but this frequency degeneracy point is detuned from the memory cavity and the atomic line, viz., $\omega_P/2 = \omega_c - \Delta\omega = \omega_a - \Delta\omega$.

It is not hard to study the effects of these two cavity detuning cases within the construct of our single-photon-error model, because their resulting density matrices are both Werner states of the form given in (94). In particular, their success probabilities are given by

$$P_{s_j} = \frac{\left[\bar{n}(1+\bar{n}) - |\tilde{n}_j|^2\right]^2 + 2|\tilde{n}_j|^2}{4\left[\bar{n}(1+\bar{n}) - |\tilde{n}_j|^2\right]^2 + 2|\tilde{n}_j|^2} \tag{125}$$

where

$$\bar{n} = I_- - I_+ \tag{126}$$

$$\tilde{n}_1 = I_- + I_+ \tag{127}$$

$$\tilde{n}_2 = I'_- + I'_+ \tag{128}$$

with

$$I_\pm = \frac{\eta_L \gamma \gamma_c}{\Gamma \Gamma_c} \times \frac{G}{(1 \pm G)\left[1 \pm G + \frac{\Gamma_c}{\Gamma} + \frac{\frac{\Delta\omega^2}{\Gamma^2}}{1 \pm G + \frac{\Gamma_c}{\Gamma}}\right]} \tag{129}$$

$$I'_\pm = \frac{\eta_L \gamma \gamma_c}{\Gamma(\Gamma_c + i\Delta\omega)} \times \frac{G}{(1 \pm G)\left(1 \pm G + \frac{\Gamma_c}{\Gamma} + \frac{i\Delta\omega}{\Gamma}\right)}. \tag{130}$$

The average teleportation fidelity, $F_j = (2P_{s_j} + 1)/3$ for $j = 1, 2$, is plotted versus normalized detuning in Fig. 10(a). We see that fidelity actually improves slightly as the normalized detuning is increased. However, this modest fidelity improvement is accompanied by a dramatic loss of singlet-state throughput, as seen in Fig. 10(b), when the detuning exceeds the OPA cavity's linewidth.

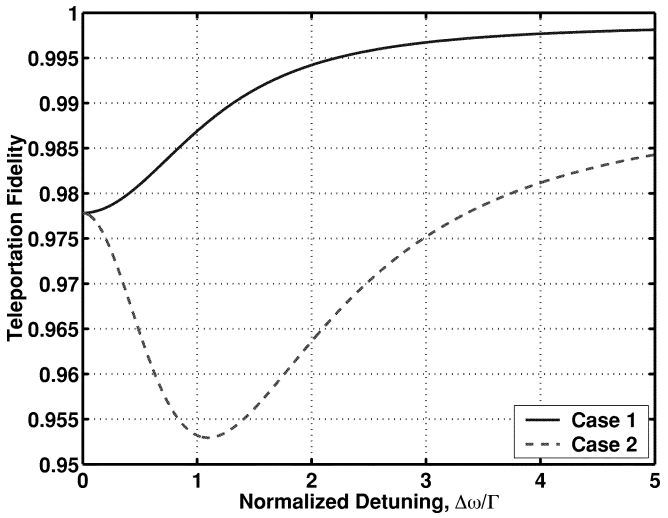

(a)

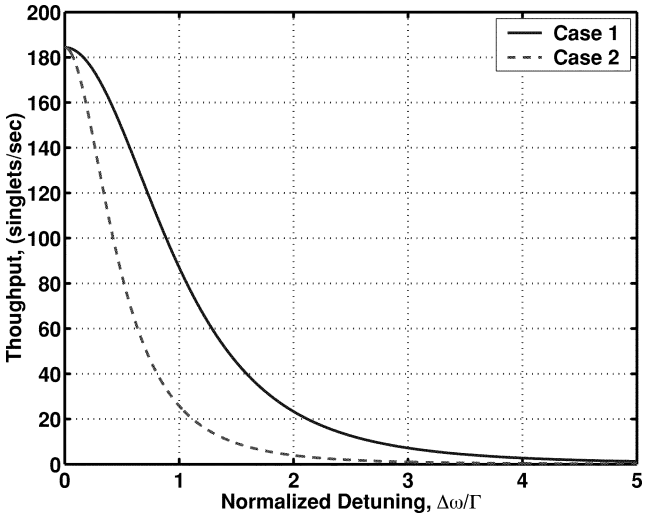

(b)

Fig. 10. (a) Teleportation fidelity versus normalized detuning, $\Delta\omega/\Gamma$. Case 1 assumes that the signal and idler center frequencies are detuned from $\omega_P/2$ with $\omega_P/2$ matched to the memory cavity resonance, ω_c, and the $^{87}\mathrm{Rb}$ atomic line, ω_a. Case 2 assumes the dual-OPA operates at frequency degeneracy, $\omega_P/2$, but this frequency is detuned from $\omega_c = \omega_a$. (b) Singlet-state throughput versus normalized detuning. We assume the loading protocol operates at a 500 kHz cycling rate. In both (a) and (b) the other parameters are the same as those for Fig. 6.

VII. Concluding Remarks

The MIT/NU quantum communication architecture is designed to enable long-distance high-fidelity qubit teleportation. It relies on a novel ultrabright source of polarization-entangled photon pairs and trapped-atom quantum memories. By means of quantum-state frequency conversion and time-division multiplexed polarization restoration, it is able to employ standard telecommunication fiber for long-distance entanglement transmission. In this paper, we have developed error models for the effects of pump amplitude, phase, and frequency errors and imperfect polarization restoration on the throughput and fidelity of the MIT/NU architecture. Our results show that this system's fidelity is not very sensitive to any of these errors. However, significant loss of singlet-state throughput may be incurred in

some circumstances even though there is no appreciable loss of fidelity.

In parallel with the theoretical work reported here, the MIT/NU team is actively working to implement its teleportation architecture. Recent progress in this regard includes demonstrations of: Total-flux polarization entanglement from a bidirectionally pumped, degenerate parametric downconverter [16]; polarization entanglement from a bidirectionally pumped, highly nondegenerate parametric downconverter [17]; efficient single-photon counting via frequency upconversion [18]; 50 km end-to-end entanglement transmission over standard telecommunication fiber [13]. The degenerate downconverter operates at 795 nm, hence providing polarization entangled pairs for local memory-loading experiments, i.e., without fiber transmission. The nondegenerate downconverter has one output at 795 nm and the other at 1.61 μm in the low-loss fiber transmission window. The short-wavelength photon from this source could be loaded into a local Rb-atom memory, while the other was transmitted through optical fiber to a distant memory. Resonated versions of these sources are presently being constructed. The upconversion system for 1.55 μm photon counting is the foundation for the quantum-state frequency converter that is currently under development. Work is also underway on the trapped Rb-atom quantum memories. Here, an integrated cavity/FORT structure has been built, and an atomic fountain scheme for loading this structure has been demonstrated [19].

REFERENCES

[1] J. H. Shapiro, "Architectures for long-distance quantum communication," *New J. Phys.*, vol. 4, pp. 47.1–47.18, 2002.

[2] C. H. Bennett, G. Brassard, C. Crépeau, R. Jozsa, A. Peres, and W. K. Wootters, "Teleporting an unknown quantum state via dual classical and Einstein–Podolsky–Rosen channels," *Phys. Rev. Lett.*, vol. 70, pp. 1895–1899, 1993.

[3] J. H. Shapiro and N. C. Wong, "An ultrabright narrowband source of polarization-entangled photon pairs," *J. Opt. B: Quantum Semiclass. Opt.*, vol. 2, pp. L1–L4, 2000.

[4] S. Lloyd, M. S. Shahriar, J. H. Shapiro, and P. R. Hemmer, "Long-distance unconditional teleportation of atomic states via complete Bell state measurements," *Phys. Rev. Lett.*, vol. 87, p. 167903, 2001.

[5] D. Bouwmeester, J.-W. Pan, K. Mattle, M. Eibl, H. Weinfurter, and A. Zeilinger, "Experimental quantum teleportation," *Nature*, vol. 390, pp. 575–579, 1997.

[6] D. Bouwmeester, K. Mattle, J.-W. Pan, H. Weinfurter, A Zeilinger, and M. Zukowski, "Experimental quantum teleportation of arbitrary quantum states," *Appl. Phys. B*, vol. 67, pp. 749–752, 1998.

[7] P. Kumar, "Quantum frequency conversion," *Opt. Lett.*, vol. 15, pp. 1476–1478, 1990.

[8] J. M. Huang and P. Kumar, "Observation of quantum frequency conversion," *Phys. Rev. Lett.*, vol. 68, pp. 2153–2156, 1992.

[9] J. H. Shapiro, "Generating quantum interference and polarization entanglement with optical parametric amplifiers," in *Proc. 6th Int. Conf. Quantum Communication, Measurement, Computing*, O. Hirota and J. H. Shapiro, Eds., Princeton, NJ, 2003, pp. 153–158.

[10] N. C. Wong, K.-W. Leong, and J. H. Shapiro, "Quantum correlation and absorption spectroscopy in an optical parametric oscillator in the presence of pump noise," *Opt. Lett.*, vol. 15, pp. 891–893, 1990.

[11] K. Bergman, C. R. Doerr, H. A. Haus, and M. Shirasaki, "Sub-shot-noise measurement with fiber-squeezed optical pulses," *Opt. Lett.*, vol. 18, pp. 643–645, 1993.

[12] J. P. Gordon and H. Kogelnik, "PMD fundamentals: Polarization mode dispersion in optical fibers," *Proc. Natl. Acad. Sci.*, vol. 97, 2000.

[13] X. Li, P. Voss, J. E. Sharping, J. Chen, and P. Kumar, "Generation and distribution of quantum entanglement in the telecom band with standard optical fiber," presented at the Digest of Frontiers in Optics, Tucson, AZ, 2003, paper WAA4.

[14] J. H. Shapiro, J. Aung, and B. J. Yen, "Quantum error models and error mitigation for long-distance teleportation architectures," presented at the Feynman Festival, College Park, MD, Aug. 2002.

[15] J. Aung, "Quantum error modeling and correction in long distance teleportation using singlet states," S.M. thesis, Mass. Inst. Technol., 2002.

[16] M. Fiorentino, G. Messin, C. E. Kuklewicz, F. N. C. Wong, and J. H. Shapiro, "Ultrabright tunable photon-pair source with total-flux polarization entanglement," in *Digest of Quantum Electronics and Laser Science Conference*, Baltimore, MD, 2003, postdeadline paper QThPDB2.

[17] F. König, E. J. Mason, F. N. C. Wong, and M. A. Albota, "Single-spatial mode coincidence measurement of photon pairs from a highly nondegenerate PPLN downconverter," presented at the Digest of Quantum Electronics and Laser Science Conference, Baltimore, MD, 2003, paper QTuB5.

[18] M. A. Albota and F. N. C. Wong, "Efficient single-photon counting at 1.55 μm via frequency upconversion," presented at the Digest of Quantum Electronics and Laser Science Conference, Baltimore, MD, 2003, postdeadline paper QThPDB11.

[19] M. S. Shahriar, private communication.

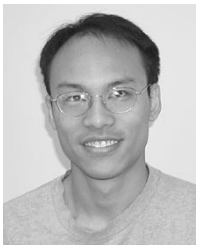

Brent J. Yen received the S.B. degrees in electrical engineering and mathematics and the M.Eng. degree in electrical engineering in 2000 from the Massachusetts Institute of Technology (MIT), Cambridge, MA. He is currently working toward the Ph.D. degree in electrical engineering at the same university.

Since 1999, he has been a Research Assistant at MIT. His research interests include quantum communications and information theory.

Jeffrey H. Shapiro (S'67–M'70–SM'84–F'95) received the S.B., S.M., E.E., and Ph.D. degrees in electrical engineering from the Massachusetts Institute of Technology (MIT) in 1967, 1968, 1969, and 1970, respectively.

As a graduate student, he was a National Science Foundation Fellow, a Teaching Assistant, and a Fannie and John Hertz Foundation Fellow. His doctoral research was a theoretical study of adaptive techniques for improved optical communication through atmospheric turbulence. From 1970 to 1973, he was an Assistant Professor of Electrical Sciences and Applied Physics at Case Western Reserve University, Cleveland, OH. From 1973 to 1985, he was an Associate Professor of Electrical Engineering at MIT, and in 1985, he was promoted to Professor of Electrical Engineering. From 1989 to 1999, he served as Associate Department Head. In 1999, he became the Julius A. Stratton Professor of Electrical Engineering. In 2001, he was appointed Director of MIT's Research Laboratory of Electronics. His research interests have centered on the application of communication theory to optical systems. He is best known for his work on the generation, detection, and application of squeezed-state light beams, but he has also published extensively in the areas of atmospheric optical communication and coherent laser radar.

Dr. Shapiro is a Fellow of the Optical Society of America and of the Institute of Physics. He is a Member of the American Physical Society and SPIE (The International Society for Optical Engineering). He has been an Associate Editor of the IEEE TRANSACTIONS ON INFORMATION THEORY and of the *Journal of the Optical Society of America*. He was the Principal Organizer of the 6th International Conference on Quantum Communication, Measurement, and Computing (QCMC'02).